ACS OMEGA

http://pubs.acs.org/journal/acsodf

Article

Crystal Chemistry, Optic and Magnetic Characterizations of a New Copper Based Material Templated by Hexahydrodiazepine

Mansoura Bourwina, Rawia Msalmi, Sandra Walha, Mark M. Turnbull, Thierry Roisnel, Ahlem Guesmi, Ammar Houas, Naoufel Ben Hamadi, and Houcine Naïli*

Cite This: *ACS Omega* 2023, 8, 15075−15082

Read Online

ACCESS | Metrics & More | Article Recommendations | Supporting Information

ABSTRACT: Crystals of the new organic−inorganic material (DAP-H2)[$CuBr_4$] (**1**); (DAP = hexahydrodiazepine ($C_5H_{14}N_2$)) were successfully synthesized by slow evaporation and characterized by single-crystal X-ray diffraction, infrared spectroscopy, thermal analysis, UV−Vis−NIR diffuse reflectance spectroscopy, and magnetic measurements. X-ray investigation demonstrates that **1** crystallizes in the monoclinic space group *C*2/*c*. The supramolecular crystal structure of **1** is guided by several types of hydrogen bonding which connect anions and cations together into a three-dimensional network. The optical band gap was determined by diffuse reflectance spectroscopy to be 1.78 eV for a direct allowed transition, implying that it is suitable for light harvesting in solar cells. The vibrational properties of this compound were studied by infrared spectroscopy, while its thermal stability was established by simultaneous TGA−DTA from ambient temperature to 600 °C. The study of the photoresponse behavior of an optoelectronic device, based on ($C_5H_{14}N_2$)[$CuBr_4$], has shown a power conversion efficiency (PCE) of 0.0017%, with J_{sc} = 0.0208 mA/cm^2, V_{oc} = 313.7 mV, and FF = 25.46. Temperature dependent magnetic susceptibility measurements in the temperature range 1.8−310 K reveal weak antiferromagnetic interactions via the two-halide superexchange pathway [$2J/k_B$ = −8.4(3) K].

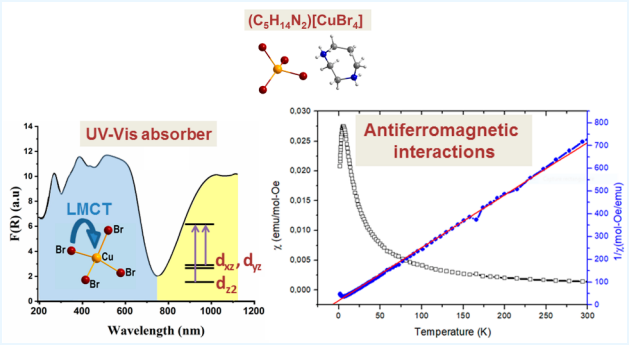

INTRODUCTION

In recent years, the scientific community has oriented toward organic−inorganic hybrid (OIH) systems which have received great interest in the industrial world thanks to their potential applications in different fields. Special attention is paid to hybrid halometalate materials, composed of metal halide anionic complexes and organic cations, due to their functional properties as well as the low cost of their preparation.[1−6] Among these materials, the hybrid perovskite family is the most famous, demonstrating high performances in photodetectors, lasers, light emitting diodes (LEDs), and photovoltaics (PVs).[7−9] For a high-quality device, a low cost and a high performance are required, and it should also be safe and nontoxic. Therefore, recent research has avoided the use of Pb-based hybrid halometalates because of their toxicity and bioaccumulation.[10] Hence, it is important to investigate low-cost and environmentally friendly hybrid halometalates. Nowadays, low-dimensional OIHs based on transition metals have been investigated as good alternatives for applications in nonhazardous devices.[11] As a consequence of the Jahn−Teller effect, these materials exhibit efficient absorption in the UV−Vis−NIR region, resulting from the electronic transitions which include both d−d transitions and ligand-to-metal charge transfer (LMCT).[12] This large absorption makes them suitable for applications in PVs as absorbers.[13,14] For example, the reported zero-dimensional compound $CH_3NH_3FeCl_4$ has demonstrated its usefulness as a photodetector and has shown a photoelectric conversion efficiency (PCE) of 0.054% when applied in the FTO/TiO_2/$CH_3NH_3FeCl_4$/carbon electrode device (FTO, fluorine-doped tin oxide).[15] Most often copper-based OIH compounds have been shown to possess interesting optical absorption. In this regard, Cu-based hybrid materials have recently emerged due to their impressive photovoltaic performance and their excellent power conversion efficiencies (PCEs). In 2015, Cui et al. investigated the two-dimensional perovskites (p-F-$C_6H_5C_2H_4NH_3)_2CuBr_4$ and $(CH_3(CH_2)_3NH_3)_2CuBr_4$ for application in heterojunction solar cells with PCEs of 0.51 and 0.63%, respectively.[16] The literature shows that the Cu(II) ion is promising, because of its d^9 configuration with its single unpaired electron, making it an S = 1/2 ion. This ion follows an external magnetic field owing

Received: December 18, 2022
Accepted: April 4, 2023
Published: April 18, 2023

to the absence of a large internal magnetic field, and it can generally be modeled as Heisenberg-like due to its *g*-factor close to 2.[17,18] In addition, depending on the separation between the inorganic layers and the distance of the M−X···X−M nonbonding contacts, magnetic properties of the hybrid compounds may vary from antiferromagnetic to ferromagnetic.[19]

(2-Amino-5-chloropyridinium)$_2$CuBr$_4$ and (2-amino-5-methylpyridinium)$_2$CuBr$_4$ have aroused interest as good examples of intralayer antiferromagnetic exchange interactions between copper(II) ions.[20] Several works were focused on metal(II) halides to study the effects of the nature of an organoammonium cation, metal, and halogen on the structural, optical, magnetic, and biological properties of the hybrid materials.[20−22] Hexahydrodiazepine and its derivatives are extensively used due to their interesting biological and pharmacological activities.[23−25]

In continuation of our previous work on OIH compounds based on transition metals, we report in this paper the crystal structure, thermal analysis, spectroscopic characterization, optoelectronic studies, and magnetic properties of the new hybrid compound (DAP-H2)[CuBr$_4$] (DAP = hexahydrodiazepine ($C_5H_{14}N_2$)) containing discrete CuBr$_4$ tetrahedra.

RESULTS AND DISCUSSION

Structural Analysis of (DAP-H2)[CuBr$_4$]. The present structure was solved in the monoclinic space group *C*2/*c* with four formula units in the unit cell. The asymmetric unit of this complex, displayed in Figure 1a, includes 1/2 $CuBr_4^{2-}$ anion

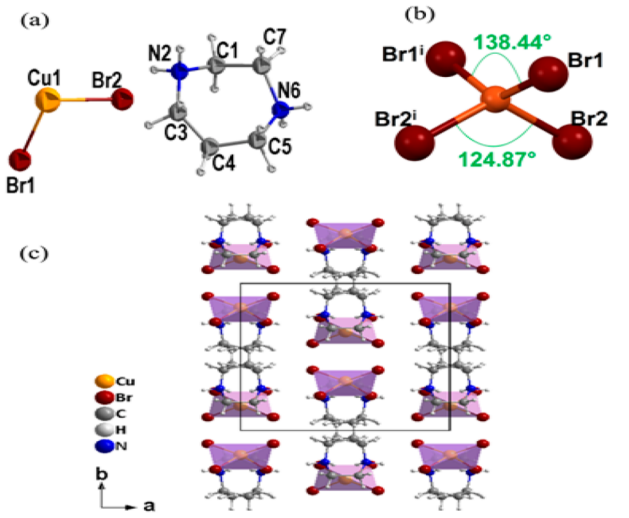

Figure 1. (a) Asymmetric unit of ($C_5H_{14}N_2$)[CuBr$_4$] showing the atom-numbering scheme. (b) Distorted tetrahedral environment of Cu^{2+} ion. (c) Projection of the atomic arrangement along the *c*-axis.

and one $(C_5H_{14}N_2)^{2+}$ cation. The hexahydrodiazepine ring lies across a 2-fold axis and was refined as a two-site disordered molecule with occupancies constrained at 50:50. The disorder of the organic cation was modeled using the EADP and SUMP constraints. All crystallographic data, measurement details, and refinement are summarized in Table S1. In the inorganic anion, the central Cu^{2+} cation is coordinated by four Br^- anions and forms a $[CuBr_4]^{2-}$ distorted tetrahedron (see Figure 1b). The inorganic part is constituted by an isolated $[CuBr_4]^{2-}$ tetrahedron with the Cu−Br bond distances varying from 2.3697(10) to 2.4049(11) Å and the Br−Cu−Br angles ranging from 99.34(3) to 138.44(8)° (Table S2), which are comparable to those found in similar structures.[26,27] With Br2i−Cu1−Br2 and Br1−Cu1−Br1i angles of 124.87(8) and 138.44(8)°, respectively, the tetrahedral $[CuBr_4]^{2-}$ ion is strongly distorted and has D_{2d} symmetry.[28] This expected distortion is due to the Jahn−Teller effect. The C−C and N−C distances range from 1.448(19) to 1.512(16) Å and from 1.473(10) to 1.490 (12) Å, respectively (Table S1). These values are close to those given for hexahydrodiazepine derivatives.[29−31] The intermolecular hydrogen bonding contacts N−H···Br provide a linkage between the $(C_5H_{14}N_2)^{2+}$ cations and the $[CuBr_4]^{2-}$ anions and give rise to a three-dimensional packing. The hydrogen bond parameters are depicted in Table S3. The N···Br distances vary from 3.351(9) to 3.637(9) Å and the N−H−Br angles range from 118 to 158°.

Thermal Behavior of (DAP-H2)[CuBr$_4$]. The thermal behavior of (DAP-H2)[CuBr$_4$] was studied by simultaneous TGA−DTA experiments, as depicted in Figure 2. The

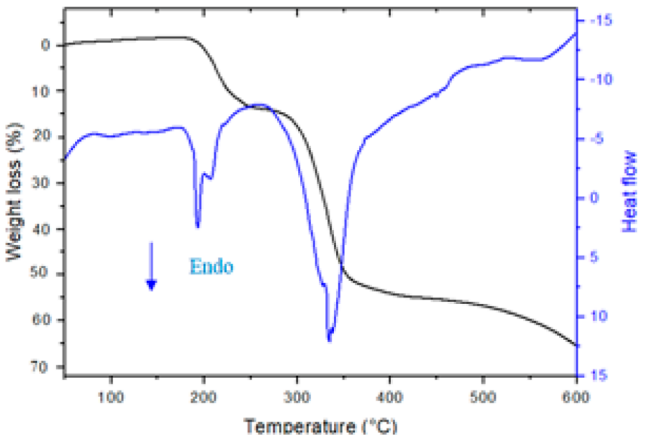

Figure 2. Simultaneous thermogravimetric analysis and differential thermal analysis scans for the decomposition of ($C_5H_{14}N_2$)[CuBr$_4$] under flowing air with a heating rate of 10 °C/min between 25 and 600 °C.

compound is totally decomposed in two stages. The first weight loss observed between 183 and 273 °C corresponds to the decomposition of the organic moiety (observed weight loss, 18%; theoretical, 21.15%). This phenomenon is accompanied by two endothermic peaks on the DTA curve at 192 and 208 °C. The second weight loss observed in the TG curve, occurring between 273 and 452 °C, is due to the loss of two HBr molecules, thus leading to the formation of the $CuBr_2$ moiety (observed weight loss, 36%; theoretical, 33%). This decomposition process is accompanied by a large endothermic peak on the DTA curve at 335 °C. The DSC analysis at low temperature was also recorded from −100 to 25 °C (Figure S1), and the material shows a phase transition between −70 and −80 °C. This transition corresponds to the order−disorder transition which is characteristic of Cu(II)-based organic−inorganic hybrid compounds.[32−34]

Optical Study. Optical properties show a good way of examining the properties of semiconductors. The diffuse reflectance spectrum (Figure 3) is translated into an absorption spectrum (Figure 4) using the Kubelka−Munk (KM) remission function (eq 1).[35]

https://doi.org/10.1021/acsomega.2c08035
ACS Omega 2023, 8, 15075−15082

$$F_{KM}(R) = (1 - R)^2/2R \quad (1)$$

where R is the reflectance of the sample.

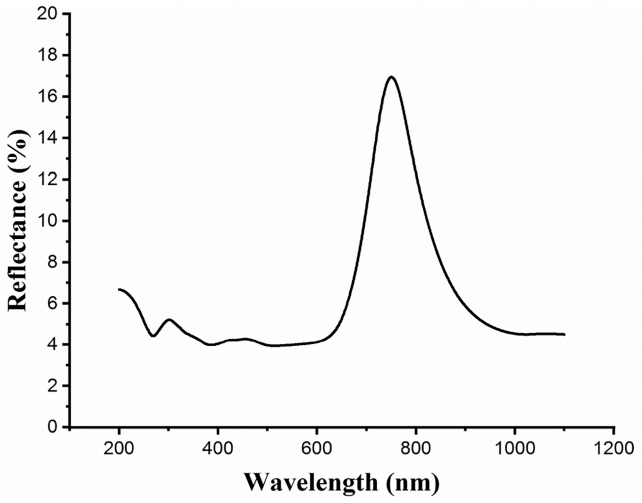

Figure 3. Reflectance spectrum of $(C_5H_{14}N_2)[CuBr_4]$.

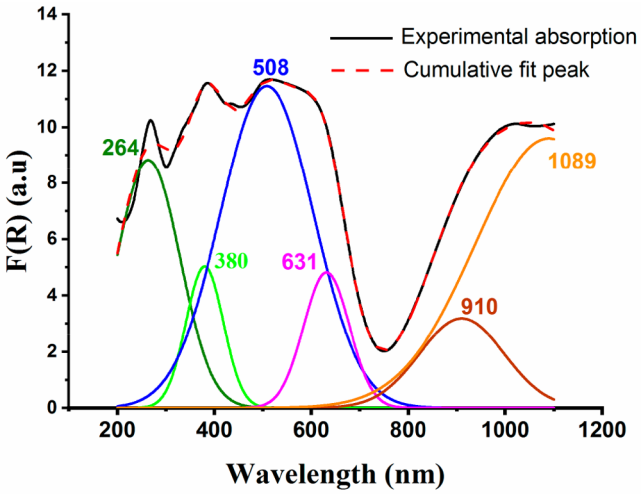

Figure 4. Multipeak Gaussian fitting of the KM absorption $F(R)$ of $(C_5H_{14}N_2)[CuBr_4]$.

A multipeak Gaussian fitting was used to characterize the possible electronic transitions within the title compound (Figure 4). The bands observed around 1000 nm are characteristic of d−d transitions within the halidocuprate(II) complex in its pseudotetrahedral D_{2d} geometry.[28] The bands at 910 and 1089 nm are assigned to the crystal field transitions from the a_1 (d_{z^2}) and e (d_{xz}; d_{yz}) orbitals to the highest energy level b_2 ($d_{x^2-y^2}$), respectively.[36] The bands located at 264, 380, 508, and 631 nm are due to the ligand−metal charge transfer (LMCT) from p-orbitals of the Br^- ligand to d-orbitals of Cu^{2+} (b_2 ($d_{x^2-y^2}$)).[36−38] Tentative assignments of the observed LMCT peaks are listed in Table 1.

For such a material, the optical band gap is one of the optical constants that have an important effect to adapt to the needs of technological components.[39] The band gap energy can be determined from the following relationship:[40]

$$[F_{KM}(R)\cdot h\nu] = B(h\nu - E_g)^n \quad (2)$$

Table 1. Assignment of Observed LMCT Electronic Transitions Compared to Those of TMA_2MnBr_4; Cu^{2+}[38]

assignment	obsd transition (nm)	transition in doped TMA_2MnBr_4; Cu^{2+}
$1a_2$ (n.b.) → $4b_2$ ($x^2 - y^2$)	631	–
4e (π) → $4b_2$ ($x^2 - y^2$)	508	555
$3a_1$ (π) → $4b_2$ ($x^2 - y^2$)	–	420
3e (π) → $4b_2$ ($x^2 - y^2$)	–	–
2e (σ) → $4b_2$ ($x^2 - y^2$)	380	352
$2a_1$ (σ) → $4b_2$ ($x^2 - y^2$)	264	277

where B is a constant, h is Planck's constant, E_g represents the optical band gap, and n is the power factor which indicates the transition mode; n equals 2 for indirect and 1/2 for direct transition natures, respectively. This value is determined by the plot of $\mathrm{Ln}[(F(R)\cdot h\nu]$ versus $\mathrm{Ln}(h\nu - E_g)$, as shown in Figure 5b and yields 1/2, which confirms the direct transition nature. The measured optical band gap energy is shown in Figure 5a. The energy band gap estimated from the linear extrapolation of $(F_{KM}(R)\cdot h\nu)^2$ values to zero absorption is 1.78 eV (inset of Figure 5a). This low value confirms that the title compound can be classified as a semiconductor material which could be used as a promising solar cell absorber material for photovoltaic applications.[11,41,42] The estimated E_g (~1.78 eV) compares well with those of Cu-based hybrids with good performances in solar cell applications, such as $(C_6H_5CH_2NH_3)_2CuBr_4$ (E_g = 1.81 eV),[41] $(CH_3NH_3)_2CuCl_2I_2$ (E_g = 1.99 eV),[11] $(CH_3NH_3)_2CuCl_2Br_2$ (E_g = 1.04 eV),[11] and $(C_6H_4NH_2)CuBr_2I$ (E_g = 1.64 eV).[42]

The behavior of the Urbach energy (E_u) can describe the degree of disorder and the defects of the structural connection of this material.[43] Equation 3 presents the Urbach rule in the low photon energy range.

$$\alpha = \alpha_0 e^{h\nu/E_u} \quad (3)$$

where α is a constant and E_u is the Urbach energy which characterizes the slope of the exponential edge. As $F(R) \propto \alpha$, eq 3 can be rewritten as eq 4.

$$F(R) = Ce^{h\nu/E_u} \quad (4)$$

where C is a constant. E_u is extracted from the inverse of the slope of the straight line of the plot of $\mathrm{Ln}(F(R))$ versus $(h\nu)$ as shown in Figure 6. The weak value of the E_u energy, 0.62 eV, indicates that our studied component is ordered.

Device Characterization. Current density−voltage (J−V) curves were recorded with a 3A Oriel solar simulator (Newport) producing 1 sun AM1.5G (100 mW cm^2). A square active area (0.09 cm^2) was used to decrease the influence of scattered light. The external quantum efficiency (EQE) measurements were carried out with a 150 W xenon lamp attached to a Bentham PVE300 motorized 1/4 m monochromator as the light source. In the concept of photovoltaic performance, the fabricated device with $(C_5H_{14}N_2)CuBr_4$ has shown a power conversion efficiency (PCE) of 0.0017%, with J_{sc} = 0.0208 mA/cm^2, V_{oc} = 313.7 mV, and fill factor (FF) = 25.46. The same measurements were performed after 4 days to check the stability and the PCE performance of this material; as a result J_{sc} and PEC losses are observed, probably due to the low stability of the material, as depicted in Figure 7a and Table 2. This low PCE value results mainly from the zero-dimensionality of the inorganic sublattice. In fact, the charge transfer within the inorganic

https://doi.org/10.1021/acsomega.2c08035
ACS Omega 2023, 8, 15075−15082

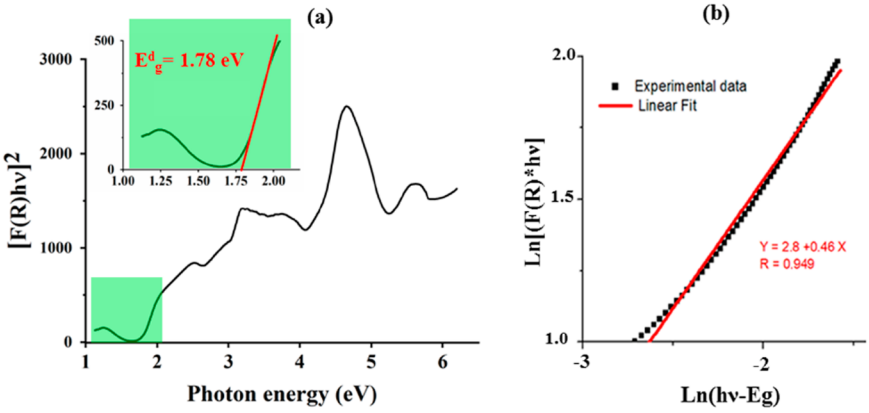

Figure 5. (a) Energy dependence of $(F(R)\cdot h\nu)^2$. (b) $(\mathrm{Ln}(F(R)\cdot h\nu)$ versus $\mathrm{Ln}(h\nu - E_g)$ of $(C_5H_{14}N_2)[CuBr_4]$.

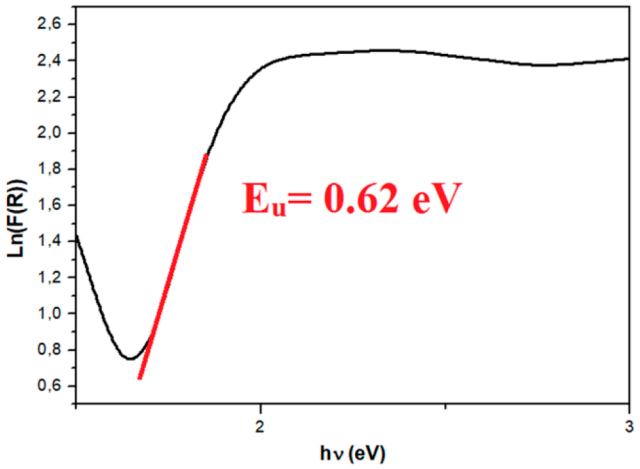

Figure 6. Determination of Urbach energy for $(C_5H_{14}N_2)[CuBr_4]$.

clusters is related to the compound dimensionality and is more important in materials with a 3D inorganic fragment than that with a low-dimensional cluster. For example, for the 3D $CH_3NH_3PbI_3$ perovskite, the PCE is about 3.8%,[44] while for the Cu-based 2D materials the highest value reached was 0.63% with $(CH_3(CH_2)_3NH_3)_2CuBr_4$.[16]

Table 2. PV Parameters of $(C_5H_{14}N_2)CuBr_4$

device	V_{oc} (mV)	J_{sc} (mA cm^{-2})	FF (%)	PCE (%)
$(C_5H_{14}N_2)CuBr_4$	313.7	0.0208	25.46	0.0017
device after 4 days	322.6	0.0112	26.72	0.001

The incident EQE (Figure 7b) measurement demonstrates a narrow absorption peak at 340 nm. The results indicate that only metal to ligand charge transfer transitions below 400 nm contribute to the photoresponsivity.

Magnetic Properties. Magnetization as a function of the applied field was measured on compound **1** from 0 to 50 kOe (see Figure S2). The magnetization reaches a value of ∼1270 emu/mol, approximately 30% of the expected saturation value for an $S = 1/2$ moment with g slightly greater than 2 as is normal for Cu(II). The response was linear to ∼8 kOe. In addition, upward curvature is observed with increasing field, indicative of a low-dimensional antiferromagnetic (AMF) lattice.[45] The magnetic susceptibility was measured from 1.8 to 310 K in an applied field of 1 kOe. A Curie−Weiss plot (see Figure S3) over the temperature range 35−300 K gave a Curie constant (CC) of 0.419(2) emu·K/mol·Oe and a Weiss constant (θ) of −3.5(7) K in agreement with the AFM interactions indicated in the $M(H)$ data. $\chi(T)$ data are shown in Figure 8. χ increases with decreasing temperature, reaching a

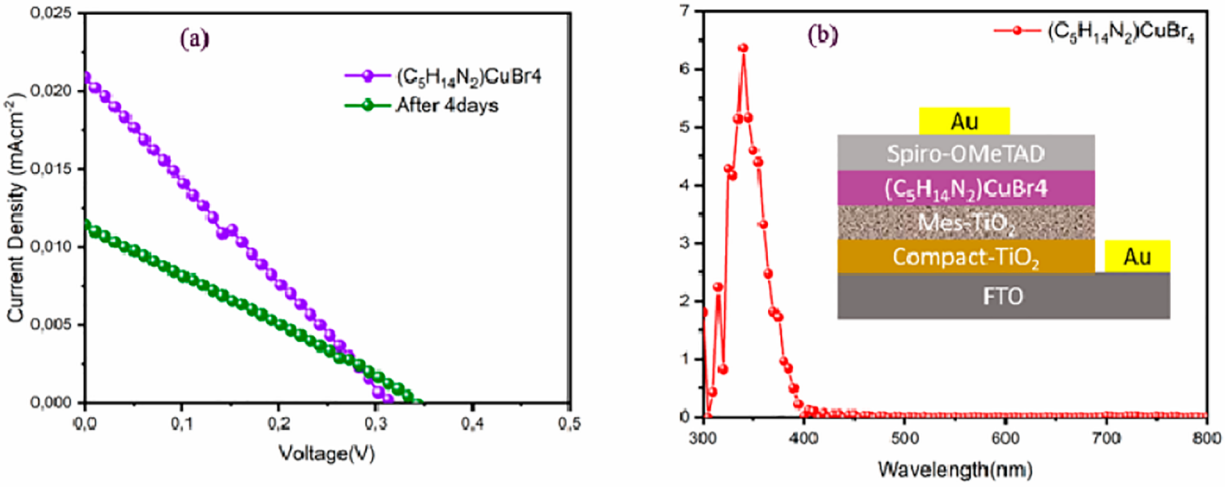

Figure 7. (a) $J-V$ curve of solar cells sensitized with $(C_5H_{14}N_2)CuBr_4$. (b) Corresponding external quantum efficiency graph with n−i−p device structure.

https://doi.org/10.1021/acsomega.2c08035
ACS Omega 2023, 8, 15075−15082

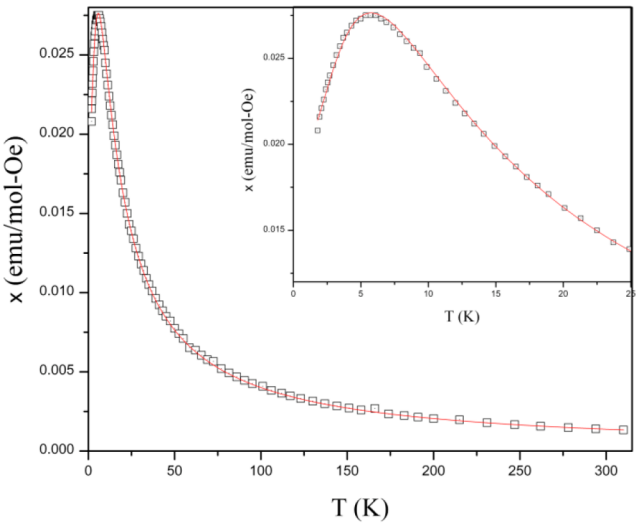

Figure 8. Susceptibility data for $(C_5H_{14}N_2)[CuBr_4]$. The solid line represents the best fit to the uniform 1D-Heisenberg chain model. The inset shows the quality of fit in the region of the maximum in χ.

maximum of 2.75×10^{-2} emu/mol·Oe at 5.7 K, before decreasing with further decrease in temperature, again indicating antiferromagnetic exchange. Such interactions were expected via the two-halide superexchange pathway as has been observed previously in many materials.[27,46,47] Examination of the structure revealed short Br··· Br contacts which generated a chain structure parallel to the *ac*-face diagonal (Figure 9) with parameters $d_{Br\cdots Br}$ = 4.197 Å, ∠Cu1−Br1···

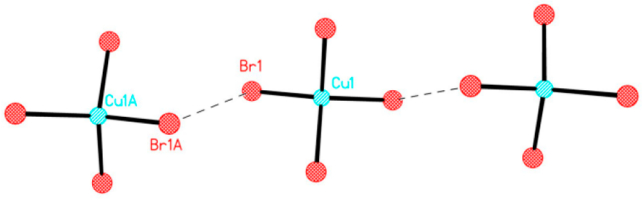

Figure 9. Chain structure formed by short Br···Br contacts in compound **1**. Symmetry operation for A = $-x + 0.5, -y + 1.5, -z + 1$.

Br1A = ∠Cu1A−Br1A···Br1 = 98.7°, and ∠Cu1−Br1···Br1A−Cu1A = 180°. Although there are several Br···Br contacts of <5.0 Å,[47] these are the shortest and are expected to dominate the interactions. A fit to the 1D-Heisenberg AFM chain model gave very reasonable values for CC [0.0417(1) emu·K/mol·Oe] and $2J/k_B = -8.7(1)$ K but required a negative percentage paramagnetic impurity (−0.85%) and an unphysical result. This indicated that additional interactions must also play a measurable role, so the data were refit to the 1D-Heisenberg AFM chain model with a Curie−Weiss correction to take interchain interactions into account. This resulted in CC = 0.420(2) emu·K/mol·Oe, $2J/k_B = -8.4(3)$ K, $\theta = -0.5(3)$ K, and a 0.9(8)% paramagnetic impurity. The small, negative Weiss constant indicates that there are indeed weak, but detectable, antiferromagnetic interactions between the chains.

CONCLUSION

In summary, this article details the synthesis of a new hybrid compound using the hexahydro-1,4-diazepine ligand, (DAP-H2)[$CuBr_4$]. Single-crystal X-ray structure determination reveals that (DAP-H2)[$CuBr_4$] crystallizes in the monoclinic space group *C*2/*c*. The structure of the synthesized material exhibits a three-dimensional supramolecular assembly where the formulary entities are stabilized by N−H···Br intermolecular hydrogen bonds. The thermal decompositions of the complex were studied by simultaneous TGA−DTA which demonstrated the thermal stability of (DAP-H2)[$CuBr_4$] up to 180 °C. The optical behavior study, using solid-state UV−Vis−NIR absorption analysis, reveals that with a band gap energy of 1.78 eV our compound is suitable for wide-band-gap top cell application in solar cells. Due to the low band gap and the stable light absorption of $(C_5H_{14}N_2)CuBr_4$, we applied this material in a solar cell device and attained a PCE of 0.0017%. In addition, the magnetic measurements in the 1.8−300 K temperature range indicated weak antiferromagnetic interactions that were well modeled by a 1D-AFM model with a small correction for interchain interactions.

EXPERIMENTAL SECTION

Materials and Synthesis. All chemicals and solvents were purchased from Sigma-Aldrich and were used as received. The solvent used in this synthesis was distilled water. (DAP-H2)[$CuBr_4$] was formed by the same method used for the preparation of $(C_5H_{14}N_2)[CuCl_4]$,[48] except that $CuCl_2$ was replaced by $CuBr_2$ and HCl was replaced by HBr. For this synthesis, 10 mL of an aqueous solution containing 0.222 g (2.223 mmol) of hexahydro-1,4-diazepine ($C_5H_{12}N_2$), 0.318 g (2.223 mmol) of copper bromide, and 0.5 mL of HBr (48%) was prepared and then stirred under heating (60 °C) for a few minutes. After room temperature evaporation of the obtained solution for a few days, black prismatic crystals were collected with a sample percent yield of 82%. Elemental analysis (C/H/N) was performed to confirm the composition of the compound. Calcd (%): C 12.37, H 2.9, N 5.77. Found: C 12.31(4), H 2.87(4), N 4.63(5). Analysis of the halogens showed that Br constituted 65.79(4)% of the sample (theoretical value 65.85%). The consistency of the experimental and theoretical mass percentages confirmed the molecular formula of the compound. The vibrational IR study confirms the existence of different functional fragments within the molecular structure. Figure S4 represents the major selected absorptions in the IR spectra of the title compound with their respective assignments (Table S3). A detailed analysis of IR and Raman spectra and assignments of all bands observed are cited in the Supporting Information.

X-ray Data Collection. Details of the crystallographic data collection and refinement parameters for the studied compound are given in Table S1. A single crystal of dimensions 0.41 × 0.25 × 0.14 mm was used for the diffraction data collection at 150 K on a D8 VENTURE Bruker AXS diffractometer using Mo Kα radiation (λ = 0.71073 Å) through the program APEX3.[49] The frame integration and data reduction were carried out with the program SAINT.[50] The program SADABS[51] was employed for multiscan type absorption corrections. The crystal structure was solved by direct methods using the SHELXT software package[52] and refined with full-matrix least-squares methods based on F^2 (SHELXL-2015).[53] All non-hydrogen atoms were anisotropically refined, and the positions of H atoms were geometrically assigned and allowed to ride on their parent atoms, with C−H = 0.97 Å and N−H = 0.89 Å. All figures were made using DIAMOND.[54]

Fabrication of the (DAP-H2)[$CuBr_4$] Optoelectronic Device. FTO-coated glass substrates were cleaned by

https://doi.org/10.1021/acsomega.2c08035
ACS Omega 2023, 8, 15075−15082

sonication in detergent. A Hellmanex solution (2%), deionized water, acetone, and isopropanol were used to clean FTO-coated glass substrates for 20 min, respectively, followed by UV−ozone treatment for 30 min. A compact blocking layer of TiO_2 was deposited on the FTO substrates by spray pyrolysis at 500 °C, employing 1/19 mL of titanium(IV) diisopropoxide bis(acetylacetonate) precursor solution (75% in 2-propanol) in pure ethanol, and then keeping them for another 30 min. After that, a 150−200 nm mesoporous TiO_2 layer was deposited by a spin-coating process. For this, a (1:8) TiO_2 paste (Dyesol 30 NR-D) diluted in ethanol for 30 s at 4000 rpm was used. The substrates were dried at 125 °C and then annealed until 500 °C in a four-step temperature ramp and maintained at 500 °C for 30 min. DMF solutions of 1 M concentration were prepared by dissolving the crystals of $(C_5H_{14}N_2)CuBr_4$ and spin coating for 30 s with 3000 rpm. They were then annealed for 30 min at 100 °C. To confirm the structural composition of the thin film, the powder XRD pattern was recorded. The convergence between the experimental pattern and the simulated one indicates that the product obtained by spin coating from the DMF solution is still the original compound (see Figure S5). Once it was cooled to room temperature, the hole transport material (HTM) layer was deposited. Spiro-OMeTAD (70 mM) was prepared by dissolving the corresponding material in 1 mL of chlorobenzene. Spiro-OMeTAD was doped by adding bis(trifluoromethylsulfonyl)-imide lithium salt (Li-TFSI) and 4-*tert*-butylpyridine (4-*t*-BP) in molar ratios of 0.5 and 3.3, respectively. HTM solutions (40 μL) were spin-coated atop the perovskite layer at 4000 rpm for 30 s, in an argon-filled glovebox. To finish the device construction, the gold cathode layer of 70 nm was thermally evaporated under a low vacuum (10−6 Torr).

Characterization Techniques. TGA−DTA measurements were obtained using a SETSYS Evolution instrument (Pt crucibles, Al_2O_3 as a reference), under nitrogen flow (100 mL/min), with a heating rate of 5 °C min^{-1} up to 600 °C. The infrared spectrum was recorded in the 500−4000 cm^{-1} range with a PerkinElmer 1600 FT-IR Spectrometer using a sample pressed in a spectroscopically pure KBr pellet. The diffuse reflectance spectrum was measured at room temperature using a Varian Cary 5000 UV−vis−NIR spectrophotometer at room temperature in the wavelength range 200−1200 nm.

Magnetic studies were conducted on a Quantum Design MPMS-XL SQUID magnetometer. Single crystals of the sample were crushed into powder and packed in a gelatin capsule. The magnetization of the sample was measured as a function of the field from 0 to 50 kOe. Several data points were collected as the field was reduced to 0 to check for hysteresis effects; none were observed. Temperature dependent magnetic susceptibility data were collected over the temperature range 1.8−310 K at an applied magnetic field of 1000 Oe. The data were corrected for the background of the sample holder (measured independently), the temperature independent paramagnetism of the Cu(II) ion, and the diamagnetic contributions of the constituent atoms as estimated via Pascal's constants.[55] The data were fit using the Hamiltonian $H = -2J\sum S_1 \cdot S_2$.

■ ASSOCIATED CONTENT

Supporting Information

The Supporting Information is available free of charge at https://pubs.acs.org/doi/10.1021/acsomega.2c08035.

Complete bond lengths and angles; IR spectroscopy; additional magnetic measurements (PDF)

■ AUTHOR INFORMATION

Corresponding Author

Houcine Naïli − *Laboratoire Physico-Chimie de l'Etat Solide, Département de Chimie, Faculté des Sciences de Sfax, Université de Sfax, 3000 Sfax, Tunisia;* orcid.org/0000-0002-9224-5851; Email: houcine.naili@fss.rnu.tn

Authors

Mansoura Bourwina − *Laboratoire Physico-Chimie de l'Etat Solide, Département de Chimie, Faculté des Sciences de Sfax, Université de Sfax, 3000 Sfax, Tunisia*

Rawia Msalmi − *Laboratoire Physico-Chimie de l'Etat Solide, Département de Chimie, Faculté des Sciences de Sfax, Université de Sfax, 3000 Sfax, Tunisia*

Sandra Walha − *Laboratoire Physico-Chimie de l'Etat Solide, Département de Chimie, Faculté des Sciences de Sfax, Université de Sfax, 3000 Sfax, Tunisia*

Mark M. Turnbull − *Carlson School of Chemistry and Biochemistry, Clark University, Worcester, Massachusetts 01610, United States;* orcid.org/0000-0002-0232-8224

Thierry Roisnel − *Institut des Sciences Chimiques de Rennes UMR 6226 CNRS, Université Rennes 1, F-35042 Rennes, France*

Ahlem Guesmi − *Chemistry Department, College of Science, Imam Mohammad Ibn Saud Islamic University, Riyadh 11432, Saudi Arabia;* orcid.org/0000-0002-7552-4146

Ammar Houas − *Research Laboratory of Catalysis and Materials for Environment and Processes, University of Gabes, 6029 Gabes, Tunisia;* orcid.org/0000-0001-8432-072X

Naoufel Ben Hamadi − *Chemistry Department, College of Science, Imam Mohammad Ibn Saud Islamic University, Riyadh 11432, Saudi Arabia; Medicinal Chemistry and Natural Products, Laboratory of Heterocyclic Chemistry, Natural Products and Reactivity (LR11ES39), Faculty of Science of Monastir, University of Monastir, 5019 Monastir, Tunisia;* orcid.org/0000-0002-2410-5275

Complete contact information is available at: https://pubs.acs.org/10.1021/acsomega.2c08035

Notes

The authors declare no competing financial interest.

■ ACKNOWLEDGMENTS

The authors extend their appreciation to the Deanship of Scientific Research at Imam Mohammad Ibn Saud Islamic University (IMSIU) for funding and supporting this work through Research Partnership Program No. RP-21-09-70.

■ REFERENCES

(1) Dolbecq, A.; Dumas, E.; Mayer, C. R.; Mialane, P. Hybrid Organic-Inorganic Polyoxometalate Compounds: From Structural Diversity to Applications. *Chem. Rev.* **2010**, *110* (10), 6009−6048.

(2) Allen, F. H.; Hoy, V. J.; Howard, J. A. K.; Thalladi, V. R.; Desiraju, G. R.; Wilson, C. C.; McIntyre, G. J. Crystal Engineering and Correspondence between Molecular and Crystal Structures. Are 2- and 3-Aminophenols Anomalous? *J. Am. Chem. Soc.* **1997**, *119* (15), 3477−3480.

(3) Sanchez, C.; Julián, B.; Belleville, P.; Popall, M. Applications of Hybrid Organic-Inorganic Nanocomposites. *J. Mater. Chem.* **2005**, *15* (35−36), 3559−3592.
(4) Desiraju, G. R. Crystal Engineering. From Molecules to Materials. *J. Mol. Struct.* **2003**, *656* (1−3), 5−15.
(5) Férey, G. Building Units Design and Scale Chemistry. *J. Solid State Chem.* **2000**, *152* (1), 37−48.
(6) Schubert, U. Cluster-Based Inorganic−Organic Hybrid Materials. *Chem. Soc. Rev.* **2011**, *40* (2), 575−582.
(7) Klejna, S.; Zawal, P.; Soo, H. S.; Mazur, T.; Wlazlak, E.; Szaciłowski, K. Halogen-Containing Semiconductors : From Artificial Photosynthesis to Unconventional Computing. *Coord. Chem. Rev.* **2020**, *415*, 213316.
(8) Zhou, C.; Lin, H.; He, Q.; Xu, L.; Worku, M.; Chaaban, M.; et al. Low Dimensional Metal Halide Perovskites and Hybrids. *Mater. Sci. Eng. R* **2019**, *137*, 38−65.
(9) Wang, J.; Liu, Y.; Han, S.; Li, Y.; Xu, Z.; Luo, J.; Hong, M.; Sun, Z.; Ma, Y. Ultrasensitive Polarized-Light Photodetectors Based on 2D Hybrid. *Sci. Bull.* **2021**, *66* (2), 158−163.
(10) Babayigit, A.; Ethirajan, A.; Muller, M.; Conings, B. Toxicity of Organometal Halide Perovskite Solar Cells. *Nat. Mater.* **2016**, *15* (3), 247−251.
(11) Elseman, A. M.; Shalan, A. E.; Sajid, S.; Rashad, M. M.; Hassan, A. M.; Li, M. Copper-Substituted Lead Perovskite Materials Constructed with Different Halides for Working (CH3NH3)-2CuX4-Based Perovskite Solar Cells from Experimental and Theoretical View. *ACS Appl. Mater. Interfaces* **2018**, *10* (14), 11699−11707.
(12) Valiente, R.; de Lucas, M. C. M.; Rodriguez, F. Polarized Charge Transfer Spectroscopy of Cu 2 + in Doped One-Dimensional [N (CH 3) 4] CdCl 3 and Polarized Charge Transfer Spectroscopy of Cu2 + in Doped One-Dimensional [N (CH3) 4] CdCl3 and [N (CH3) 4] CdBr3 Crystals. *J. Phys.: Condens. Matter* **1994**, *6*, 4527−4540.
(13) Valiente, R.; Rodriguez, F. Comment on "Copper-Substituted Lead Perovskite Materials Constructed with Different Halides for Working (CH3NH3)2CuX4-Based Perovskite Solar Cells from Experimental and Theoretical View. *ACS Appl. Mater. Interfaces* **2020**, *12* (34), 37807−37810.
(14) Cortecchia, D.; Dewi, H. A.; Yin, J.; Bruno, A.; Chen, S.; Baikie, T.; Boix, P. P.; Gratzel, M.; et al. Lead-Free MA 2 CuCl x Br 4-x Hybrid Perovskites. *Inorg. Chem.* **2016**, *55*, 1044−1052.
(15) Yin, J.; Shi, S.; Wei, J.; He, G.; Fan, L.; Guo, J.; Zhang, K.; Xu, W.; Yuan, C.; Wang, Y.; Wang, L.; Pu, X.; Li, W.; Zhang, D.; Wang, J.; Ren, X.; Ma, H.; Shao, X.; Zhou, H. Earth-Abundant and Environment Friendly Organic-Inorganic Hybrid Tetrachloroferrate Salt CH3NH3FeCl4: Structure, Adsorption Properties and Photoelectric Behavior. *RSC Adv.* **2018**, *8* (36), 19958−19963.
(16) Cui, X. P.; Jiang, K. J.; Huang, J. H.; Zhang, Q. Q.; Su, M. J.; Yang, L. M.; Song, Y. L.; Zhou, X. Q. Cupric Bromide Hybrid Perovskite Heterojunction Solar Cells. *Synth. Met.* **2015**, *209*, 247−250.
(17) Herringer, S. N.; Turnbull, M. M.; Landee, C. P.; Wikaira, J. L. Synthesis, Structure, and Magnetic Properties of Bis(3-Amino-2-Chloropyridinium)Tetrahalocuprate(II) [Halide = Cl or Br]. *J. Coord. Chem.* **2009**, *62* (6), 863−875.
(18) Storr, A.; Summers, D. A.; Thompson, R. C. Transition Metal Azolates from Metallocenes. Part 3: Polymeric Manganese(II) and Nickel(II) Pyrazolates; Synthesis, Characterization, and Magnetochemistry. *Can. J. Chem.* **1998**, *76* (8), 1130−1137.
(19) Manaka, H.; Yamada, I.; Yamaguchi, K. Ferromagnetic-Dominant Alternating Heisenberg Cains with Ferromegnetic and Atiferromagnetic Interactions Formed in (CH3)2CHNH3CuCl3. *J. Phys. Soc. Jpn.* **1997**, *66*, 564−567.
(20) Woodward, F. M.; Albrecht, A. S.; Wynn, C. M.; Landee, C. P.; Turnbull, M. M. Two-Dimensional S = 1/2 Heisenberg Antiferromagnets: Synthesis, Structure, and Magnetic Properties. *Phys. Rev. B - Condens. Matter Mater. Phys.* **2002**, *65* (14), 144412.
(21) Msalmi, R.; Elleuch, S.; Hamdi, B.; Abd El-Fattah, W.; Ben Hamadi, N.; Naili, H. Organically Tuned White-Light Emission from Two Zero-Dimensional Cd-Based Hybrids. *RSC Adv.* **2022**, *12*, 10431.
(22) Hfidhi, N.; Krayem, N.; Erwann, J.; Bataille, T.; Naïli, H. Lamellar and Supramolecular Feature of New Tutton's Salts Incorporating 2-Amino-4-Methylpyrimidine: Thermal Stability, Optic Study, Antioxidant and Antimicrobial Activities. *J. Inorg. Organomet. Polym. Mater.* **2021**, *31* (4), 1549−1564.
(23) Mazimba, O. Antimicrobial Activities of Heterocycles Derived from Thienylchalcones. *J. King Saud Univ. - Sci.* **2015**, *27* (1), 42−48.
(24) Stankiewicz, K.; Bobrański, B.; Tatarczyńska, E.; Chojnacka-Wójcik, E. New Hexahydro[1,4]Diazepine-7H-5,7-Diones with Potential Neurotropic Activity. *Farmaco. Sci.* **1984**, *39* (12), 1038−1049.
(25) Sprio, V.; Caronna, S.; Migliara, O.; Petruso, S.; Matera, M. Synthesis of pyrazolo[3,4-e][1,4]diazepine-4,7-diones with central nervous system activity. *Farmaco* **1989**, *44* (9), 809−818.
(26) Coomer, F. C.; Bondah-Jagalu, V.; Grant, K. J.; Harrison, A.; McIntyre, G. J.; Rønnow, H. M.; Feyerherm, R.; Wand, T.; Meißner, M.; Visser, D.; McMorrow, D. F. Neutron Diffraction Studies of Nuclear and Magnetic Structures in the S = 1/2 Square Heisenberg Antiferromagnets (D6 −5CAP)2 Cu X4 (X = Br and Cl). *Phys. Rev. B - Condens. Matter Mater. Phys.* **2007**, *75* (9), 1−11.
(27) Woodward, F. M.; Landee, C. P.; Giantsidis, J.; Turnbull, M. M.; Richardson, C. Structure and Magnetic Properties of (5BAP)-2CuBr4: Magneto-Structural Correlations of Layered S = 1/2 Heisenberg Antiferromagnets. *Inorg. Chim. Acta* **2001**, *324* (1−2), 324−330.
(28) Czekański, Ł.; Hoffmann, S. K.; Barczyński, P.; Gąsowska, A.; Zalewska, A.; Goslar, J.; Ratajczak-Sitarz, M.; Katrusiak, A. Syntheses, Crystal Structures and Spectroscopic Studies of Bis[1-Methyl-3-(Methoxycarbonylmethyl)-Benzimidazolium]2+[CuBr4]2−and [ZnBr4]2−Compounds. *ChemistrySelect* **2017**, *2* (34), 11120−11130.
(29) Said, M.; Boughzala, H. Structural Characterization and Physicochemical Features of New Coordination Polymer Homopiperazine-1,4-Diium Tetrachlorocadmate(II). *J. Mol. Struct.* **2020**, *1220*, 128696.
(30) Shi, Q. Z.; Xing, Z.; Cao, Y. N.; Ma, S. B.; Chen, L. Z. Synthesis, Structure and Dielectric Properties of a Cd Coordination Polymer Based on Homopiperazine. *J. Mol. Struct.* **2017**, *1130*, 363−367.
(31) Ayari, C.; Alotaibi, A. A.; Baashen, M. A.; Alotaibi, K. M.; Alharbi, K. H.; Othmani, A.; Fujita, W.; Nasr, C. B.; Mrad, M. H. Synthesis of New Homopiperazine-1.4-Diium Tetrachloridromercurate (II) Monohydrate (C5H14N2)[HgCl4]·H2O, Crystal Structure, Hirshfeld Surface, Spectroscopy, Thermal Analysis, Antioxidant Activity, Electric and Dielectric Behavior. *Crystals* **2022**, *12*, 486.
(32) Willett, R. D.; Haugen, J. A.; Lebsack, J.; Morrey, J. Thermochromism in Copper(II) Chlorides. Coordination Geometry Changes in Tetrachlorocuprate(2-)Anions. *Inorg. Chem.* **1974**, *13* (10), 2510−2513.
(33) Asghar, M. A.; Zhang, S.; Khan, T.; Sun, Z.; Zeb, A.; Ji, C.; Li, L.; Zhao, S.; Luo, J. Reversible Phase Transition Driven by Order-Disorder Transformations of Metal-Halide Moieties in [(C6H14)-NH2]2·CuBr4. *J. Mater. Chem. C* **2016**, *4* (32), 7537−7540.
(34) Bloomquist, D. R.; Willett, R. D. Thermochromic Phase Transitions in Transition Metal Salts. *Coord. Chem. Rev.* **1982**, *47* (1−2), 125−164.
(35) Dang, Y.; Liu, Y.; Sun, Y.; Yuan, D.; Liu, X.; Lu, W.; Liu, G.; Xia, H.; Tao, X. Bulk Crystal Growth of Hybrid Perovskite Material CH3NH3PbI3. *CrystEngComm* **2015**, *17* (3), 665−670.
(36) Desjardins, S. R.; Penfield, K. W.; Cohen, S. L.; Solomon, E. I.; Musselman, R. L. Detailed Absorption, Reflectance, and UV Photoelectron Spectroscopic and Theoretical Studies of the Charge-Transfer Transitions of CuCl42-: Correlation of the Square-Planar and the Tetrahedral Limits. *J. Am. Chem. Soc.* **1983**, *105* (14), 4590−4603.

https://doi.org/10.1021/acsomega.2c08035
ACS Omega 2023, 8, 15075−15082

(37) Massabni, A. C.; Nascimento, O. R.; Halvorson, K.; Willett, R. D. Synthesis, Structure, and Electronic and EPR Spectra of Copper(II) Complexes Containing the [CuBr4]2- Anion and Triphenylarsine Oxide. *Inorg. Chem.* **1992**, *31* (10), 1779−1784.
(38) de Lucas, M. C. M.; Rodriquez, R. Luminescence Properties of Cu -Doped TMA 2 MnBr 4 Crystals and a Spectroscopic Study of the CuBr 42- Complexes Formed. *J. Phys.: Condens. Matter* **1993**, *5*, 2625.
(39) Sanchez, C.; Lebeau, B.; Chaput, F.; Boilot, J. Optical Properties of Functional Hybrid Organic-Inorganic Nanocomposites. *Adv. Mater.* **2003**, *15*, 1969−1994.
(40) Duvenhage, M.; Ntwaeaborwa, M.; Visser, H. G.; Swarts, P. J.; Swarts, J. C.; Swart, H. C. Determination of the Optical Band Gap of Alq 3 and Its Derivatives for the Use in Two-Layer OLEDs. *Opt. Mater. (Amst)* **2015**, *42*, 193−198.
(41) Wu, J.; Li, X.; Liu, X.; Wu, S.; Lai, W. Y.; Zheng, Y. Effects of Conjugated Bridges on the Photovoltaic Properties of: Ortho -Functionalized Perylene Diimides for Non-Fullerene Polymer Solar Cells. *J. Mater. Chem. C* **2018**, *6* (48), 13171−13178.
(42) Li, X.; Zhong, X.; Hu, Y.; Li, B.; Sheng, Y.; Zhang, Y.; Weng, C.; Feng, M.; Han, H.; Wang, J. Organic-Inorganic Copper(II)-Based Material: A Low-Toxic, Highly Stable Light Absorber for Photovoltaic Application. *J. Phys. Chem. Lett.* **2017**, *8* (8), 1804−1809.
(43) Studenyak, I.; Kranjec, M.; Kurik, M. Urbach Rule in Solid State Physics. *Int. J. Opt. Appl.* **2014**, *4* (3), 76−83.
(44) Kojima, A.; Teshima, K.; Shirai, Y.; Miyasaka, T. Organometal Halide Perovskites as Visible-Light Sensitizers for Photovoltaic. *JACS Commun.* **2009**, *131*, 6050−6051.
(45) Landee, C. P.; Turnbull, M. M. Review: A Gentle Introduction to Magnetism: Units, Fields, Theory, and Experiment. *J. Coord. Chem.* **2014**, *67* (3), 375−439.
(46) Dgachi, S.; Ben Salah, A. M.; Turnbull, M. M.; Bataille, T.; Naïli, H. Investigations on (C6H9N2)2[MIIBr4] Halogenometallate Complexes with MII = Co, Cu and Zn: Crystal Structure, Thermal Behavior and Magnetic Properties. *J. Alloys Compd.* **2017**, *726*, 315−322.
(47) Turnbull, M. M.; Landee, C. P.; Wells, B. M. Magnetic Exchange Interactions in Tetrabromocuprate Compounds. *Coord. Chem. Rev.* **2005**, *249* (23), 2567−2576.
(48) Bourwina, M.; Msalmi, R.; Walha, S.; Turnbull, M. M.; Roisnel, T.; Costantino, F.; Mosconi, E.; Naïli, H. A New Lead-Free 1D Hybrid Copper Perovskite and Its Structural, Thermal, Vibrational, Optical and Magnetic Characterization. *J. Mater. Chem. C* **2021**, *9* (18), 5970−5976.
(49) *APEX3*, ver. 2015.5-2; Bruker AXS Inc.: Madison, WI, USA, 2015.
(50) *SAINT*, ver. 8.34A; Bruker AXS Inc.: Madison, WI, USA.
(51) *SADABS*, ver. 2014/5; Bruker AXS Inc.: Madison, WI, USA.
(52) Sheldrick, G. ShelXT-Integrated Space-Group and Crystal-Structure Determination. *Acta Crystallogr.* **2015**, *A71*, 3−8.
(53) Sheldrick, G. M. Crystal Structure Refinement with *SHELXL*. *Acta Crystallogr. Sect. C Struct. Chem.* **2015**, *71* (1), 3−8.
(54) Brandenburg, K.; Putz, H. *Diamond: Crystal and Molecular Structure Visualization*; Crystal Impact: Bonn, Germany, 2008.
(55) Carlin, R. L. *Magnetochemistry*; Springer-Verlag: 1986.

https://doi.org/10.1021/acsomega.2c08035
ACS Omega 2023, 8, 15075−15082